CCFE
CULHAM CENTRE FOR FUSION ENERGY

UK Atomic Energy Authority

UKAEA-CCFE-PR(22)47

J. Lovell, M. L. Reinke, A. R. Field, B. A. Lomanowski,
the MAST Upgrade team

Overview and first measurements of the MAST Upgrade bolometer diagnostic

Overview and first measurements of the MAST Upgrade bolometer diagnostic

J. Lovell, M. L. Reinke, A. R. Field, B. A. Lomanowski, the MAST Upgrade team

This is a preprint of a paper submitted for publication in Review of Scientific Instruments

Overview and first measurements of the MAST Upgrade bolometer diagnostic

J. Lovell,[1, 2, a)] M. L. Reinke,[1, 3] A. R. Field,[2] B. A. Lomanowski,[1] and The MAST Upgrade Team[2]

[1)] *Oak Ridge National Laboratory, Oak Ridge, TN 37831, USA*

[2)] *United Kingdom Atomic Energy Authority, Culham Centre for Fusion Energy, Culham Science Centre, Abingdon, Oxon, OX14 3DB, UK*

[3)] *Commonwealth Fusion Systems, Cambridge, MA 02139, USA*

(Dated: 28 September 2022)

A suite of multi-channel resistive bolometers have been implemented to measure the total radiation from MAST Upgrade plasmas, with cameras covering the core plasma and lower divertor chamber. Data is digitised and processed using novel FPGA-based electronics, offering improved compactness and new operational capabilities. A synthetic diagnostic has been developed to explore the quality of 2D reconstructions available from the system and to quantify the uncertainty on quantities such as the total radiated power. Measurements in the first campaign have demonstrated correct functioning of the diagnostic while also highlighting issues with electrical noise and some failure mechanisms of the detectors, as well as significant neutral beam fast-particle losses.

[a)] lovelljj@ornl.gov

I. INTRODUCTION

Power loss via short wavelength photon emission is an important factor in the overall power balance in fusion devices. Next generation devices will require large fractions of the input power to be radiated, primarily in the divertor, to avoid damage to the plasma facing components (PFCs). ITER for example is expected to require 60 % to 70 % of the total loss power to be radiatively dissipated, and DEMO will require $> 95\%$ radiative dissipation[1]. Inferring the power crossing the separatrix by measuring the core radiated power loss sets an important boundary condition for on-going divertor physics research and is expected to be a necessary component of control of future power producing reactors[2].

Bolometers are widely used in fusion experiments to provide absolute measurement of the power radiated by the plasma, integrated over a wide energy range from visible light to soft X-ray emission. The bolometer system implemented on MAST Upgrade (MAST-U) uses arrays of resistive bolometers to provide measurements of the radiated power in both the main chamber and lower divertor of the device. The bolometers will be used in a range of physics studies on MAST Upgrade, such as exploring the effectiveness of the new Super-X divertor to dissipate the loss power into the divertor through radiation and charge exchange losses and the presence of impurity radiation from the core plasma and its effect on confinement. A prototype infrared video bolometer (IRVB) which complements the resistive bolometer has also been deployed on MAST-U and is the subject of a companion paper[3].

This paper describes the resistive bolometer diagnostic as implemented in MAST Upgrade for its first experimental campaign. It is organised into several sections. Firstly the diagnostic hardware is described in Sections II A and II B, including both the in-vessel sensors and the ex-vessel acquisition electronics. Analysis of the theoretical performance and coverage of the system using a synthetic diagnostic framework is presented in Section II C. The first measurements made using the system are presented in Section III, illustrating the capabilities and challenges experienced in the first campaign. Future plans to enhance the diagnostic's capabilities are then discussed in Section IV, based on learning outcomes from the initial operation of the diagnostic.

II. HARDWARE

A. In-vessel hardware

The sensors used in the diagnostic are compact, 4-channel integrated units of foil resistive bolometers, first developed in 1991[4]. Each channel features 2 foils, one exposed to the plasma radiation and one shielded from it. Each foil is thermally-connected to a pair of meander resistors, such that the 4 resistors form a Wheatstone bridge. Plasma radiation heats the exposed foil which in turn heats the two exposed meander resistors on opposite sides of the bridge: the increase in resistance due to the temperature rise of these resistors unbalances the bridge and this bridge imbalance is measured by applying an AC excitation voltage across one diagonal of the bridge and measuring the voltage across the other diagonal. This sensor design is in widespread use in tokamaks[5]. These sensors are grouped into cameras: one camera is sited at the midplane (figure 1) and views the main chamber, and two cameras view the lower divertor chamber from the baffle (figure 2) and the outer wall (figure 3) respectively.

The main chamber bolometers use gold absorbers on a kapton substrate, since this was the standard construction of these sensors when the system was installed on MAST in 2001. The divertor bolometers use platinum absorbers on a SiN substrate, based on the design intended for use on ITER at the time the system was designed[6]. Neither the main chamber nor the divertor bolometers are blackened, so the reflectivity of the foils at lower photon energies needs to be considered when interpreting the data from each system[7]. In particular, relating measurements between the two systems is complicated by the different reflectivities of gold[8] and platinum[9].

Figure 4 shows the viewing geometry of the system. A significant fraction of the poloidal cross section of the plasma is covered through the combination of the main chamber poloidal array and the lower divertor arrays. The combination of vertical and horizontal viewing channels in the divertor arrays enable tomographic reconstructions of the measured brightness profiles to produce 2D emissivity profiles in the lower divertor. For many of the plasmas run in the first MAST Upgrade campaign — which were typically low elongation ($\kappa \sim 1.8$ to 2.2) — the X points are viewed by the main chamber array, though in subsequent campaigns where the vertical control has been optimised it is anticipated that higher elongation plasmas

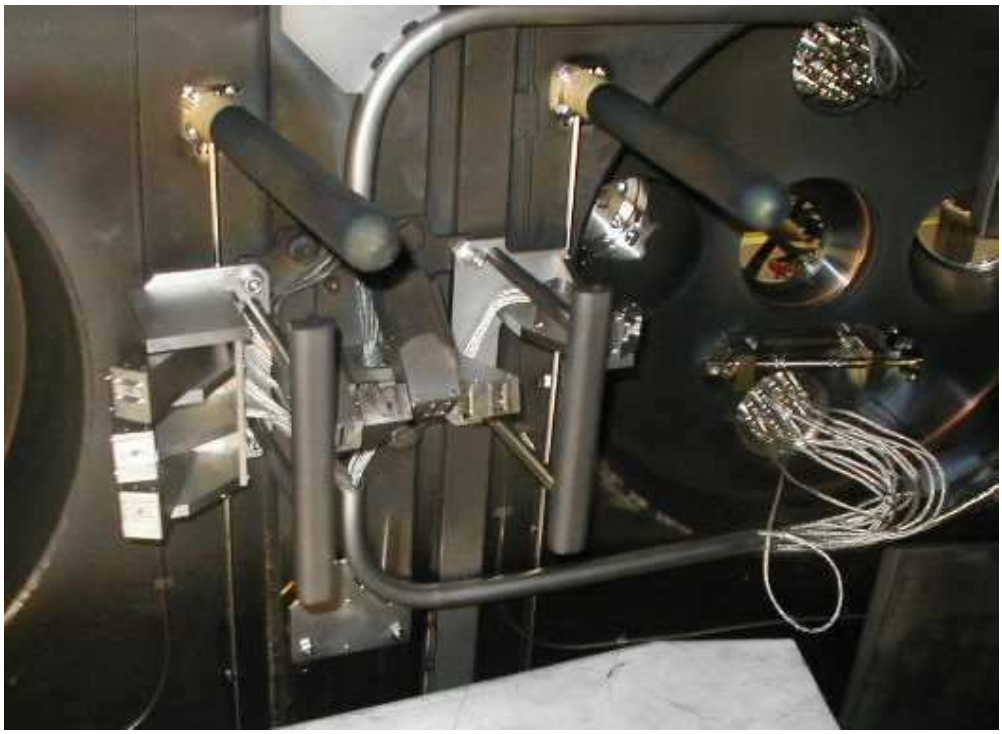

FIG. 1: The main chamber bolometer camera, as installed in MAST. Each 4-channel sensor is housed in a metal box. 3 sensors — 12 channels — provide a tangential view at the midplane in the same direction as the plasma current (seen on the left). 1 sensor — 4 channels — provides a tangential view in the opposite direction to the plasma current (right). 4 sensors in a 16-channel fan cover the poloidal cross section of the core plasma. For MAST Upgrade this same camera is used in the same location, but radially offset 10 cm from the wall.

($\kappa \sim 2.5$) will be typical and thus the X points will be closer to the divertor plates and thus out of the view of the core array. There is a region around the divertor throat where neither the core nor divertor arrays have coverage. There is also no coverage of the upper divertor for the first MAST-U campaign, though an upper divertor bolometer is to be installed for the second campaign.

B. Ex-vessel hardware

The in-vessel bolometer sensors are connected to the data acquisition electronics by screened twisted pair cables. The sensors are earthed to the vessel through the bolome-

FIG. 2: Baffle-mounted bolometer camera, before installation. There are two apertures, each viewed by 2 4-channel sensors. A plate (not shown) sits between the apertures and sensors to prevent light from the wrong aperture reaching the sensor. The plate is ridged, and all the internal surfaces of the camera and blackened, to reduce internal reflections.

ter cameras, and the screen in approximately one quarter of the length of the cable run is earthed to the same single earth point through the same camera as the sensor. The electronics are bonded to the same earth reference as the sensors in a different location, and the remaining three quarters of the length of the cable run screen is earthed through the electronics. At the join between the two parts of the cable the earth is broken by using an insulating connector to avoid a ground loop.

The data acquisition system uses recently-developed compact electronics based on FPGA technology; the electronics is described in detail in other publications[10,11]. This system provides an AC excitation voltage to the sensors, digitises the output voltage and performs digital signal processing of the received signal. The drive frequency of the AC excitation is configurable and can be set to any frequency up to 61 kHz in approximately 1 Hz intervals to reduce the impact of narrow band noise pickup. Digital signal processing recovers the output amplitude of the bridge voltage through AC synchronous detection, and the low-pass filters

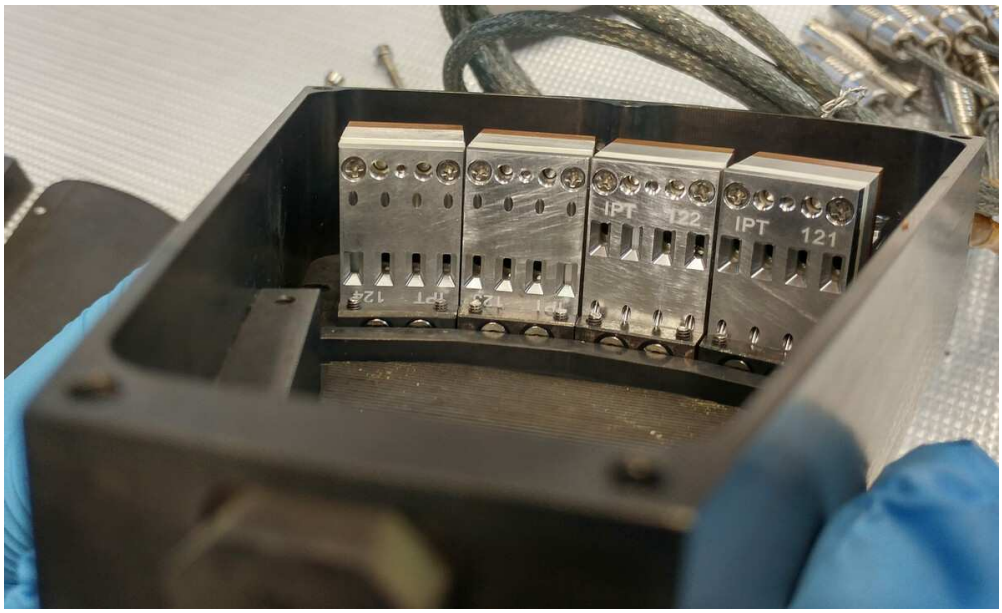

FIG. 3: Wall-mounted bolometer camera, partly disassembled. The design principle is the same as for the baffle-mounted camera shown in figure 2. The distance between the sensors and slits is larger to give a narrower field of view, and the anti-reflection ridges are present on both top and bottom of the device as well as the middle: the lower ridging can be seen in this image.

used in this process can be configured with any user-supplied cut-off frequency up to 5 kHz. This enables the system to optimise, on a shot by shot basis, the trade-off between signal-to-noise and time resolution. Furthermore, a parallel data pathway in the signal processing pipeline enables real-time calculation of the power incident on the bolometer sensors using per-channel deconvolution filters, which makes the system suitable for integration into real-time control systems to provide feedback control of the plasma radiation.

The use of FPGA technology has several advantages. The integration of all the device logic onto a single chip and the digitisation of the processing pipeline mean the system is very compact: up to 48 channels can be integrated into a single 1U, 19 in unit. In fact MAST-U uses 2 of these units, each with 32 channels, for the core and divertor systems. A full 64-channel system therefore only takes up 2U of cubicle space. The flexibility of the programmable logic and Linux-based firmware in the chip provides a highly configurable system as described above, and also enables system upgrades with new features and enhancements without having to replace the hardware.

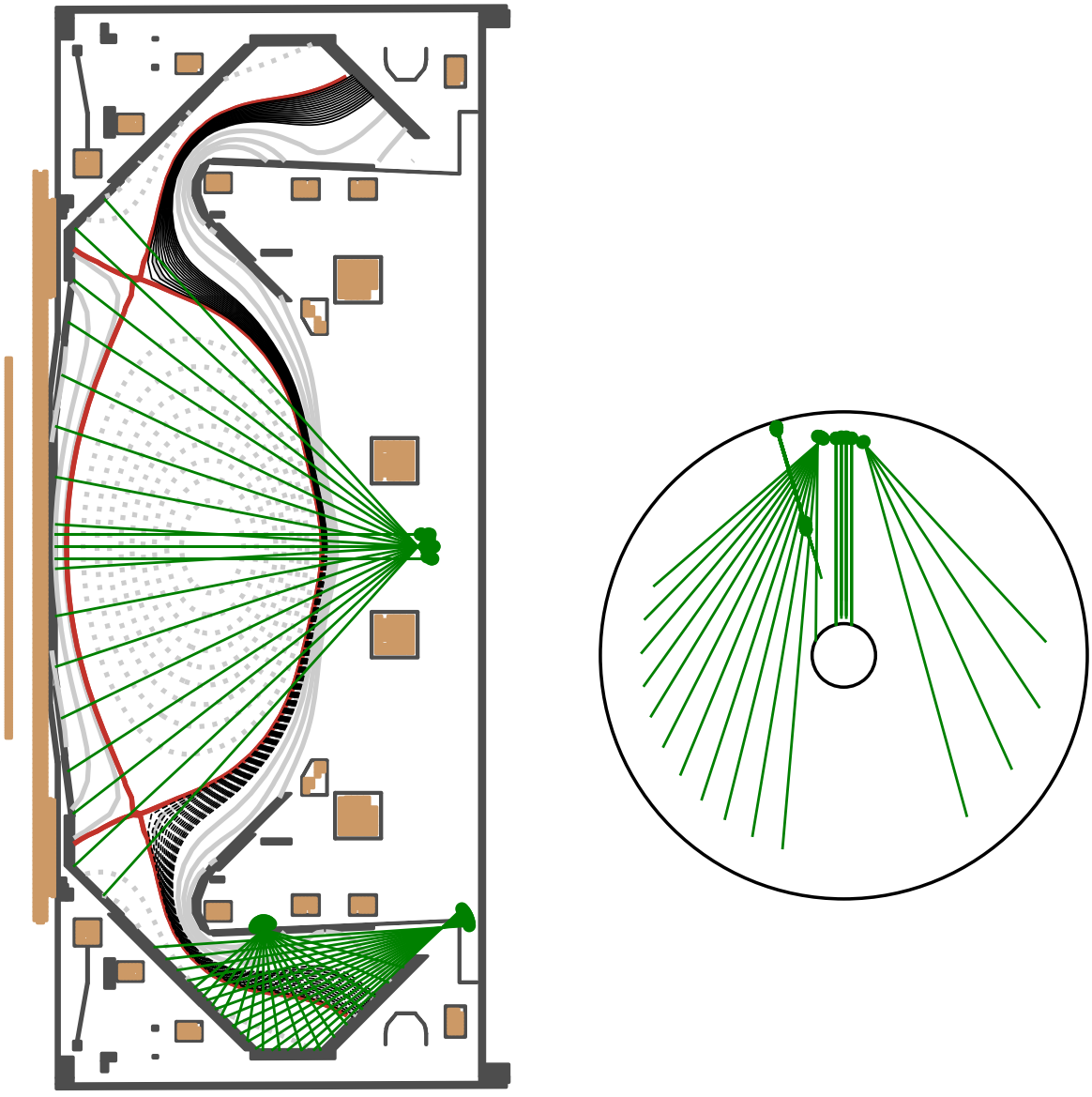

FIG. 4: Viewing geometry of the bolometer system in the MAST Upgrade vessel, with a representative Super-X divertor (SXD) magnetic equilibrium for context. Left: poloidal cross section of the viewing geometry. The main chamber poloidal fan covers the core and X points of this low-elongation shot, though in shots with higher elongation the X points are typically out of view. The lower divertor array provides good coverage of the entire SXD chamber. There is a region around the lower divertor throat which has no resistive bolometer coverage at all, and there is no coverage in the upper divertor at this time. Right: plan view of the viewing geometry. 12 tangential lines of sight view in the same direction as the plasma current and NBI injection. 4 channels provide a counter-NBI view.

The electronics also provides a mechanism to calibrate the bolometer sensors in-situ. The procedure is described in detail in reference[11] and is summarised here for convenience. A DC voltage is applied across both diagonals of the Wheatstone bridge in the sensor, such that there is a voltage difference across each of the two resistors in contact with the exposed foil and no voltage difference across the resistors in contact with the reference foil. This arrangement allows a current to flow through the measurement resistors to provide Ohmic heating with a known power. At the same time the AC excitation voltage is applied and the amplitude of the bridge output is measured. This electrical configuration is shown schematically in Figure 5.

The change in output voltage amplitude with Ohmic power determines the sensitivity S (in V/W) of the foil, and the time constant of the reduction in voltage when the Ohmic heating is switched off determines the cooling time τ (in s) of the foil. These quantities can then be used in the bolometer equation to calculate the incident power on the foil P given a measured voltage amplitude V:

$$P = \frac{1}{S}\left(V + \tau\frac{\mathrm{d}V}{\mathrm{d}t}\right) \tag{1}$$

The advantage of this method is that no correction for AC effects or foil operating temperature need to be applied: the foil voltage measurement is made in the same way as in regular operation making the calibration highly representative of plasma operation.

One other important feature to note is the AC synchronous detection is done in quadrature. The output voltage from the sensor is of the form:

$$V = A\sin(\omega t - \phi) \tag{2}$$

A is the amplitude, ω is the drive frequency and ϕ is the phase delay due to capacitance in the signal cables. We calculate the in-phase (I) and quadrature-phase (Q) components of the signal by multiplying it by a reference signal of the same frequency and filtering out the 2ω component:

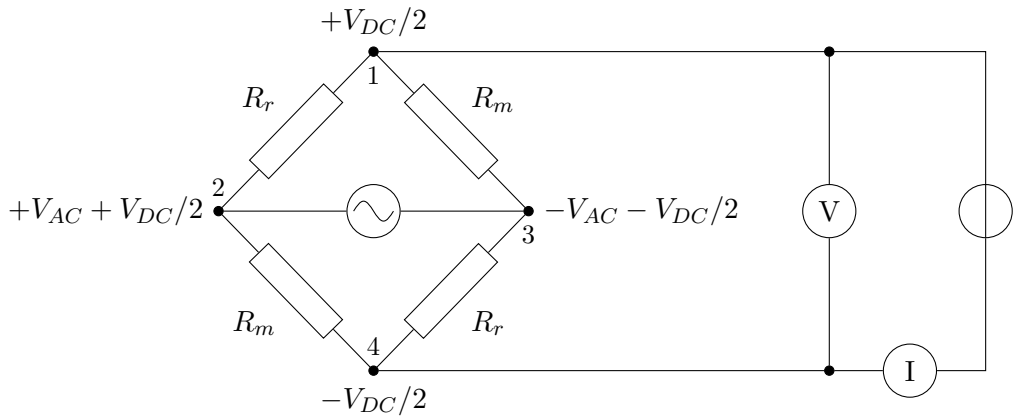

FIG. 5: Electrical schematic for the calibration procedure. A DC voltage is applied across both diagonals of the bridge, such that current flows through the resistors thermally-connected to the measurement foil R_m and not through the resistors connected to the reference foil R_r. The current Ohmically heats the foil: the Ohmic heating power is calculated by measuring the DC voltage and current. The resulting amplitude of the AC bridge output voltage is used to calculate the sensitivity of the foil. Taken from reference[11].

$$\begin{aligned} I &= \frac{1}{2n\pi}\int_0^{2n\pi} V\sin(\omega t)\,\mathrm{d}\omega t \\ &= \frac{1}{2n\pi}\int_0^{2\pi} A\sin(\omega t-\phi)\sin(\omega t)\,\mathrm{d}\omega t \\ &\approx \frac{A}{2}\cos(\phi) \end{aligned} \tag{3}$$

$$\begin{aligned} Q &= \frac{1}{2n\pi}\int_0^{2\pi} V\cos(\omega t)\,\mathrm{d}\omega t \\ &= \frac{1}{2n\pi}\int_0^{2\pi} A\sin(\omega t-\phi)\cos(\omega t)\,\mathrm{d}\omega t \\ &\approx -\frac{A}{2}\sin(\phi) \end{aligned} \tag{4}$$

For integer n the final two simplifications are exact, but even for non-integer $n \gg 1$ the approximation error is small. In practice this is achieved by ensuring the filter cut-off frequency is significantly less than the excitation frequency.

From equations 3 and 4 the amplitude and phase can be extracted:

$$A = 2\sqrt{I^2+Q^2} \tag{5}$$

$$\phi = \tan^{-1}\left(\frac{-Q}{I}\right) \tag{6}$$

Both amplitude and phase are recorded. This means the voltage can be treated as a complex quantity:

$$V = Ae^{-i\phi} \tag{7}$$

Post-processing operations such as smoothing the voltage, removing offsets — non-zero voltage at zero input power, typically due to intrinsic imbalances in the bridge resistances — and differentiating for use in the bolometer equation can be applied to this complex signal in the same way as traditionally one might treat a real voltage. The amplitude of the resulting voltage and power signals is the physical quantity of interest.

Recording both the in-phase and quadrature components means that no manual hardware correction of the phase is required: the correction can be applied in post-processing. The calibration process enables calculation of the components of the "offset voltage" and these can be applied during the signal processing pipeline stage if post-shot offset correction is not practical (for example, when the system is used for real-time feedback control).

C. Synthetic diagnostic analysis

A synthetic diagnostic model of the bolometer cameras has been developed using the Cherab framework[12]. 3D CAD models of MAST-U — including the PFCs and in-vessel coils — and the bolometer assemblies are used to produce the model. The model allows us to calculate the field of view of each channel in 3D, incorporating volumetric line of sight effects. With this information we can produce geometry matrices for use in tomographic reconstructions of the plasma emissivity, accurate calculations of the detector étendues and forward-modelled measurements of synthetic plasma emissivities.

Figure 6 shows the result of calculating the geometry matrix on a grid of toroidally-symmetric volume elements ("voxels") with rectangular poloidal cross sections, for a single channel. The grid cells closest to the detector have high weights concentrated in a small area, and the weights then reduce as the field of view spreads out further from the detector. Previous work has shown that proper consideration of the finite volume of the detector field of view reduces the need for additional regularisation when performing tomographic

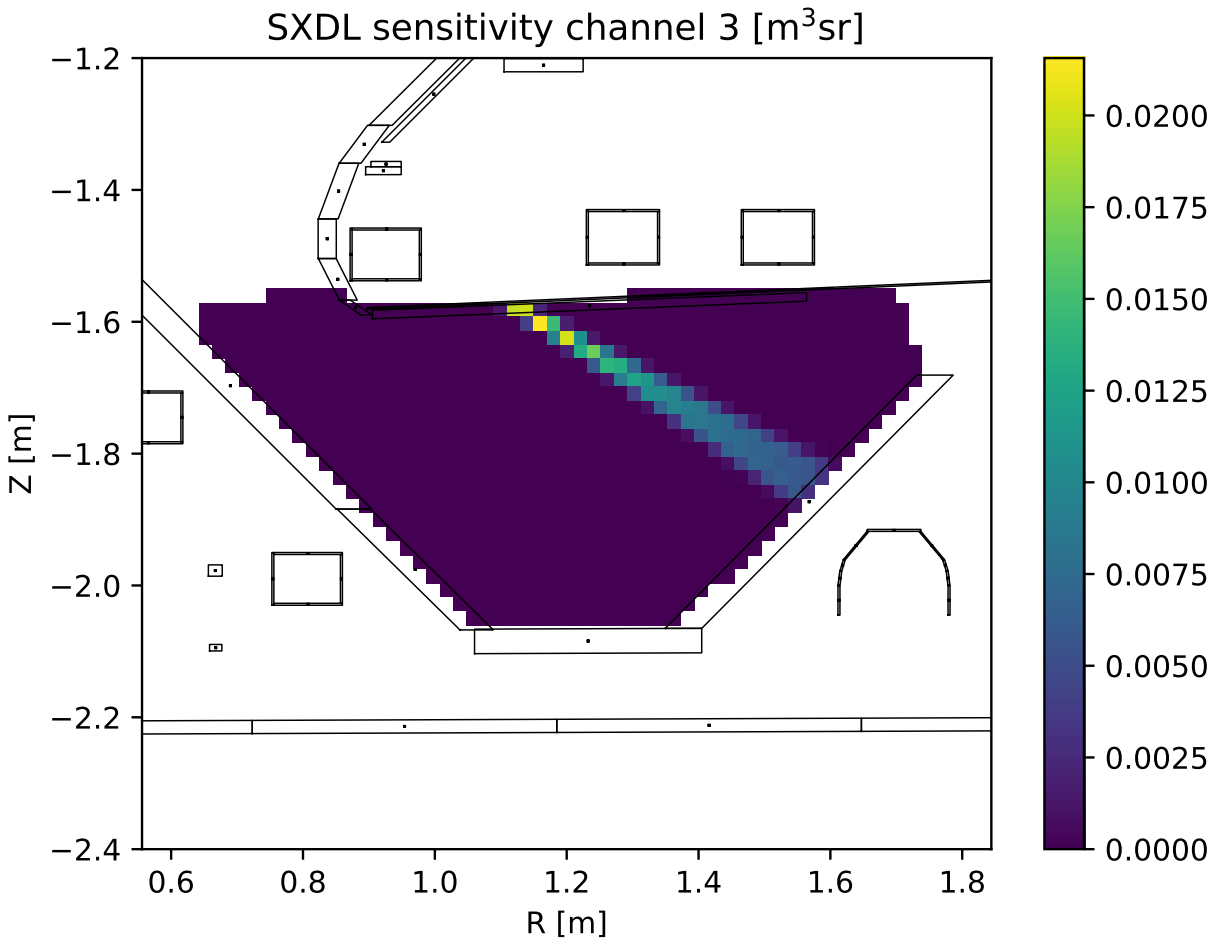

FIG. 6: Geometry matrix for one of the divertor channels. The diverging field of view of the detector is accounted for within Cherab.

inversions of measured line-integral brightness profiles and so more accurately represents the spatial resolution of the system[13].

Figure 7 shows the result of summing the geometry matrix weights for all channels in both the core and divertor regions. This illustrates the full volumetric extent of the viewing geometry in a way that the approximation using single lines of sight does not. It complements figure 4 and shows that the system covers the majority of the main and lower Super-X chambers, with a gap in coverage around the divertor throat.

The étendue of the detectors has also been calculated with Cherab, using a ray tracing method[13]. For comparison, the étendue G calculated using the following widely-used approximation is also plotted:

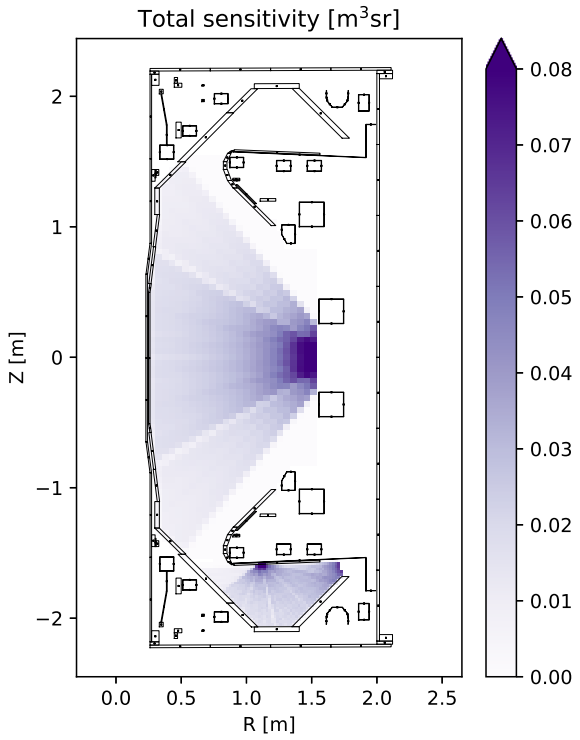

FIG. 7: Sum of all the geometry matrix weights for all channels in the system, illustrating the true extent of the coverage of the diagnostic. Note the gaps in coverage around the upper and lower divertor throat, and the reduced sensitivity around $(R, Z) = (0.8, -1.7)$ where the conventional divertor leg is typically found.

$$G = \frac{A_{det} A_{ap} \cos(\theta_{det}) \cos(\theta_{ap})}{d^2} \tag{8}$$

Here, A_{det} and A_{ap} are the areas of the foil detector and slit aperture respectively, θ_{det} and θ_{ap} are the angles between a vector from the detector to the aperture and the normal vectors of the detector and aperture respectively and d is the distance between the foil and the slit.

The results are shown in figure 8. Generally the two methods are in good agreement for the core arrays, but the analytic model under-estimates the étendue for the divertor arrays by approximately 5%. The divertor sensors have slightly more rounded openings in front of the foils which reduces the effective foil area. The étendue of the counter-NBI tangential sensors in the core are also under-estimated by the analytic model compared with the rest

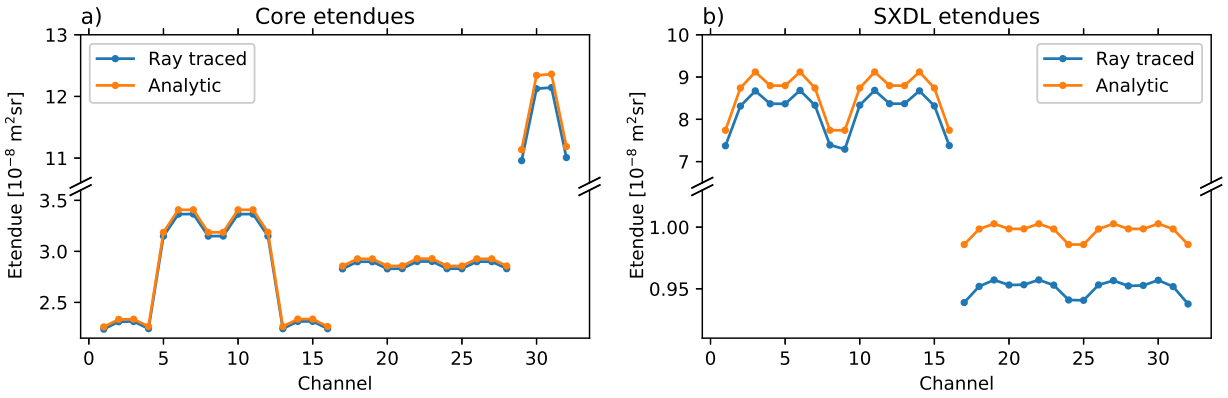

FIG. 8: Detector étendues for (a) the main chamber poloidal (channels 1–16) and tangential (channels 17–32) bolometers, and (b) the lower divertor baffle-mounted (channels 1–16) and wall mounted (channels 17–32) bolometers, as calculated by Cherab and compared with a simple analytic model. The analytic model performs well for the main chamber bolometers, but over-estimates the étendue by about 5% for the divertor bolometers.

of the core sensors. These have a smaller separation between aperture and detector and so the higher order terms which have been neglected in equation 8 become more important. This behaviour matches what has been observed in previous work[13]. Accounting for these effects is important as we seek to minimise the systematic error on the calculation of the brightness measurements, which depend linearly on the étendue.

Using the calculated geometry matrices and étendues, we can forward-model the bolometer measurements for a range of radiation emissivity profiles. The use of synthetic profiles — phantoms — with known metrics such as the total and mean position and size of the radiation means we can assess the quality of reconstructions possible with the system. This technique additionally provides a means of quantifying the uncertainties on calculated metrics such as the total radiated power, either by directly integrating the reconstructed emissivity profile or using simplified calculations such as a weighted sum of brightness measurements[14].

Uncertainty quantification has recently been performed using this technique on data from the JET tokamak[15], where the total radiated power metric was computed for a large number of phantoms of varying positions and shapes. Here we focus on only a couple of phantoms to illustrate the expected performance and limitations of the system, with a full systematic scan left for future work. Figure 9 shows an example of a phantom and the inversion of the

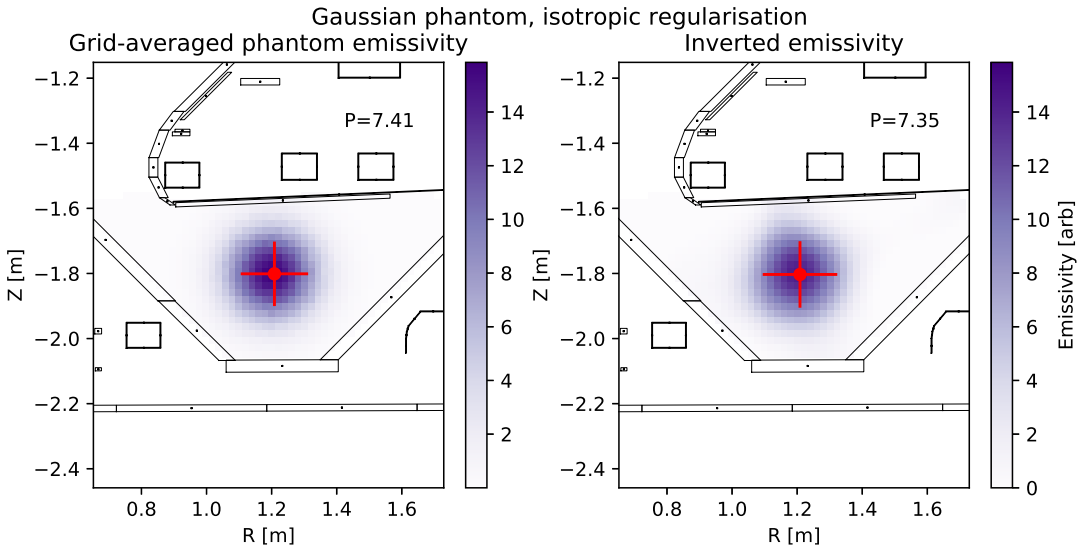

FIG. 9: A phantom with a bi-variate Gaussian emissivity profile (left) and the inversion of synthetic brightness profiles calculated from the phantom using Cherab (right). The emissivity profile itself, along with the total power, mean position and size metrics, are well reproduced by the inversion.

forward-modelled brightness profile. Gaussian phantoms such as these were generated by using an emissivity ϵ parameterised by mean radius r_0, mean height z_0, width $\mathrm{d}r$ and height $\mathrm{d}z$ as follows:

$$\epsilon(r,z) = \frac{1}{2\pi \mathrm{d}r\mathrm{d}z} \exp - \left(\frac{r-r_0}{2\mathrm{d}r^2} + \frac{z-z_0}{2\mathrm{d}z^2} \right) \tag{9}$$

This particular example used $r_0 = 1.2\,\mathrm{m}$, $z_0 = -1.8\,\mathrm{m}$, $\mathrm{d}r = 0.1\,\mathrm{m}$, $\mathrm{d}z = 0.1\,\mathrm{m}$. Synthetic brightness profiles were produced using the synthetic model of the bolometers implemented with Cherab, and then these were inverted using a non-negative least squares routine with Tikhonov regularisation[16] using a Laplacian second derivative operator as the regularisation operator as has been done in previous work[13]. The regularisation operator was chosen by hand through an iterative process to minimise the amount of regularisation while avoiding the presence of strong artefacts in the reconstruction.

From both the phantom and the inversion, we compute the zeroth order (total power), first order (mean position) and second order (width and height) moments of the emissivity distribution. For this particular case of an "isotropic" phantom (i.e. one which has similar spatial variation in both the R and Z dimensions), the emissivity profile itself and all its

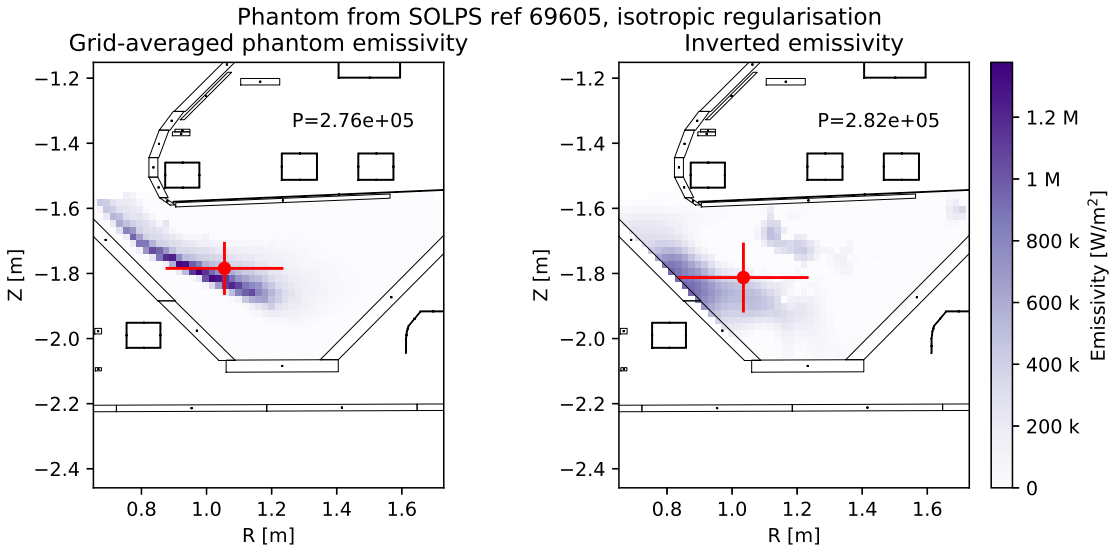

FIG. 10: A phantom from a SOLPS simulation of a MAST-U plasma with a Super-X divertor and 5 MW of NBI heating (left), and the tomographic inversion of its synthetic brightness profiles (right) using isotropic regularisation. The total power and mean position of the radiation is well reproduced, but the higher order moments and the 2D profile are not.

moments are well reproduced by the inversion. While not necessarily representative of expected emissivity profiles in the divertor chamber, this simple Gaussian example does at least provide a useful test of the workflow and suggest there are no fundamental issues with its capability to reconstruct large scale 2D radiation profiles and report the total radiated power.

To study more realistic radiation profiles we turn to predictive SOLPS simulations of MAST-U plasmas. In the rest of this subsection we focus in particular on a simulation of an L-mode, Super-X plasma with 5 MW of NBI heating power[17]. We take as the radiation profile the sum of the line emission and recombination for all species in the simulation, neglecting the impact of charge-exchange neutrals on the bolometers. Figure 10 shows the results of inverting this phantom using the same regularisation operator as in the Gaussian case above. While the total power and mean position of the phantom are rather well reproduced in the inversion, the spatial extent and the structure of the distribution are not. The inversion shows the radiation much closer to the divertor target tiles than in the phantom, and with a larger poloidal spread. This is unsurprising, as the phantom is very anisotropic and so

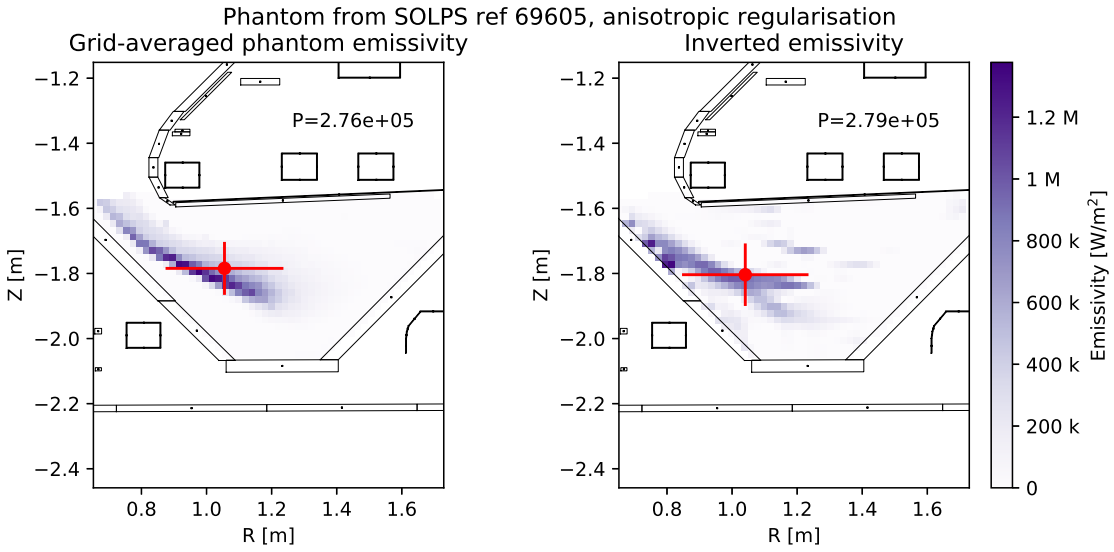

FIG. 11: The same phantom as in Figure 10, now inverted using anisotropic regularisation. The spatial distribution of the phantom is better reconstructed than in the isotropic case, and both lower and higher order moments of the distribution are well reproduced.

attempting to find a solution which maximises isotropic smoothness is unlikely to lead to a high fidelity reconstruction. However, the good agreement of the lowest order moments indicate that a standard Laplacian regularisation operator may still be useful as a general technique when only these global quantities are of interest.

We can improve the reconstruction of higher order moments by exploiting a-priori knowledge of the anisotropy of the phantom. Figure 11 shows a reconstruction of the same phantom's brightness profiles where the isotropic 2D regularisation operator has been replaced with one which encourages more smoothness in the direction parallel to the poloidal magnetic field lines than the perpendicular direction. This anisotropic regularisation technique has previously been successfully applied to bolometer tomographic reconstructions on other devices[18]. We can see now that not only are the moments of the distribution well-reproduced, the 2D profile itself is also faithfully reconstructed with the exception of a few artefacts.

The inversions presented so far use regularisation parameters hand-tuned for optimal results. This is a labour-intensive effort which requires a-priori knowledge of the result, and therefore is not practical for routine analysis. Figure 12 shows the same SOLPS phantom inverted using anisotropic regularisation, but using the FTIKREG[19] algorithm which au-

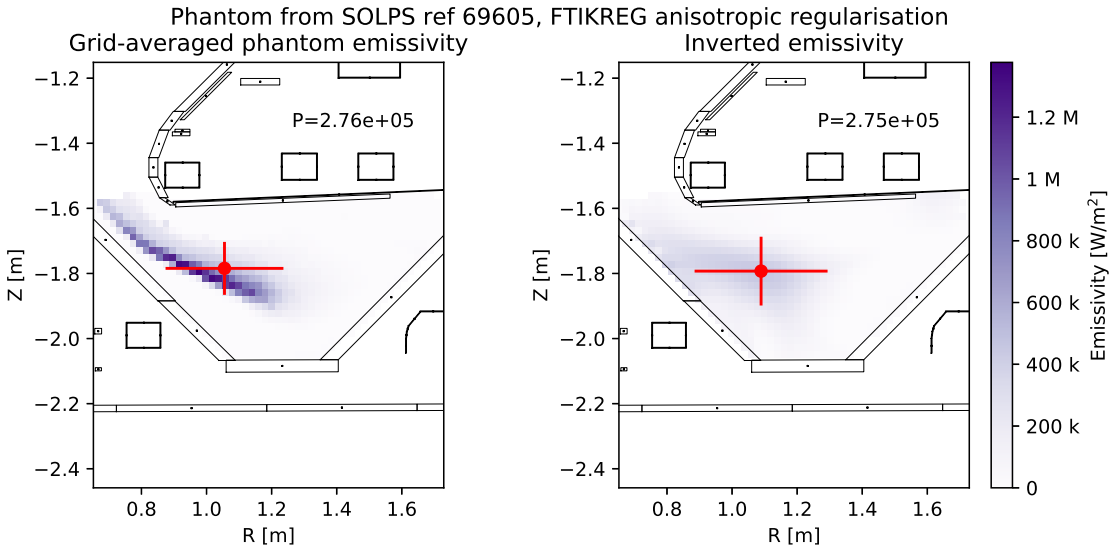

FIG. 12: The same phantom as in Figure 11, with an inversion using anisotropic regularisation and a regularisation parameter automatically determined using the FTIKREG algorithm. The inversion is more heavily smoothed than the manually-tuned inversion, but again reproduces the moments and general shape of the emissivity distribution.

tomatically determines a suitable regularisation parameter. This enables an unsupervised analysis which is more feasible to perform on a routine basis, say for an entire experimental campaign data set. With a nominal estimate of the errors of 0.5% — a best case scenario since real data will likely have higher errors than this, even heavily smoothed — the inversion algorithm produces an emissivity profile whose moments are again in good agreement with the input phantom. The profile itself is rather smoothed out, but this is not unexpected since these highly anisotropic phantoms are pushing the spatial resolution of the diagnostic to the limits. This final example is perhaps closest to what one might expect when routine tomographic inversions of MAST-U data become available.

It is important to note that these examples are representative only and not an exhaustive study of the system's limits. While the results are encouraging, they rely on a number of idealised assumptions such as minimal measurement noise, no loss of individual channels and radiation distributions positioned optimally within the field of view. In reality it is anticipated that the bolometry may more reliably function as a consistency check for radiation structures, confirming a modelled emissivity distribution is possible within measurement

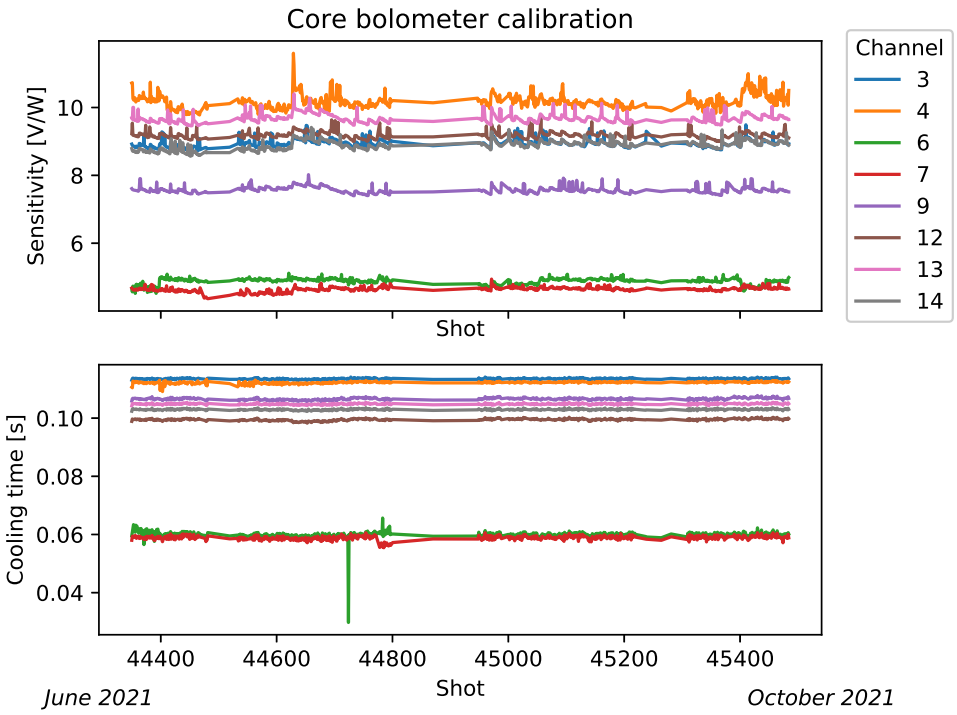

FIG. 13: Trends of the bolometer sensitivity (top) and cooling time (bottom) over time, for several channels in the core array. The calibration values show good stability over the entire shot range, which spanned several months.

uncertainty without being able to fully disprove the hypothesised radiation structure in detail.

III. MEASUREMENTS IN THE FIRST MAST UPGRADE EXPERIMENTAL CAMPAIGN

A. Calibration stability

The calibration procedure described in Section II B and external references[11] is routinely performed in about 1 minute before every MAST-U shot. This enables an analysis of the variation of the foil calibration over time as the condition of the sensors, vessel and external environment (temperature and humidity for example) evolve. Repeated calibrations also provide good statistics for evaluating the uncertainty in the calibration parameters due to noise in the voltage and current measurements and imperfect fits of the cooling curves.

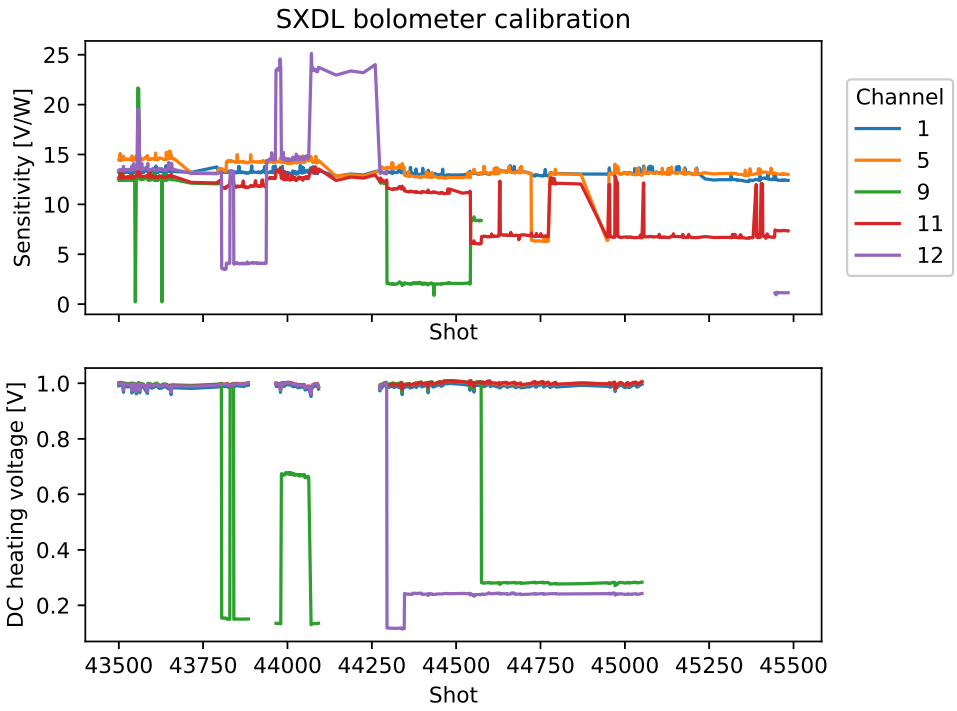

FIG. 14: Sensitivity and applied DC heating voltage for a selection of lower divertor bolometer channels over a large range of shots. Hardware failures of individual channels can be observed through sudden changes in the sensitivity. The drop in DC heating voltage indicates the failure is likely related to a partial short circuit in the system.

Figure 13 shows the bolometer sensitivity and cooling time calibration values, obtained from fits of the recorded calibration data, for many shots over a period of 3 months, for a representative sample of main chamber channels. There are clearly visible differences in the calibration parameters between channels, due variations in the manufacturing process of the individual bolometer chips, with channels 6 and 7 in particular coming from a much older sensor which was used to replace previously failed hardware when the array was re-used for MAST Upgrade. However, the individual channels all show only small variations in both the sensitivity and cooling time, with the former having slightly more scatter than the latter across all channels. The scatter provides a useful quantification of the real world uncertainty on these calibration parameters (and therefore on the uncertainty of the measured radiated power). For the period and channels shown in Figure 13 we obtain fractional uncertainties of $\frac{\delta S}{S} = 1\,\%$ to $2\,\%$ and $\frac{\delta \tau}{\tau} = 0.1\,\%$ to $0.4\,\%$.

Another advantage of performing the calibration before every shot is that it provides

almost continuous monitoring of the state of the system. This means that when faults occur they can be identified quickly and easily. By way of example, Figure 14 shows the sensitivity values for a selection of channels in the baffle-mounted camera in the lower divertor. In contrast to the main chamber bolometers, these bolometers show sudden large changes in the sensitivity which indicate a problem with the channels. Looking at the average measured DC Ohmic heating voltage applied during the calibration, we can see that some of these channels experienced a sudden drop in the applied voltage, which hints at a partial short circuit in the bolometer chip. This was confirmed by multimeter measurements at the vacuum feedthrough after the failures were observed in routine data analysis.

We can pinpoint the date and (in some cases) the first shot number after the failure of these channels, which may aid in the determination of the cause of these faults. For example, sudden calibration changes after a particularly large disruption, or some other off-normal event such as the plasma divertor strike point position striking unintended surfaces or rapid pressure changes, could indicate the cause of a failure and the likely damage. In this instance, nothing unexpected was observed in plasma shots around the time of the failures of these particular channels but the capability is still useful to have for future operations.

B. Routine measurements

We present here some examples of measurements routinely made by the diagnostic in the first campaign. A key quantity is the total radiated power; this is calculated for both the core and divertor arrays using a weighted sum of brightness measurements[14]. We report separately the total radiated power measured by the core and lower divertor arrays. For the core, the 16 poloidal channels are used. For the lower divertor, the 16 baffle-mounted, vertically-viewing channels were used in the first MAST-U experimental campaign. We would ideally use the wall-mounted horizontally-viewing channels[20], but hardware failures (see Section III E for details) precluded this and necessitated post-campaign repairs.

Figure 15 shows some examples of the total measured radiated power for three different plasma scenarios, with both conventional and Super-X divertors and Ohmic and NBI heating. Due to the viewing geometry in the divertor, the measured divertor radiation in conventional divertor shots is very low and almost certainly significantly lower than the total emitted radiation along the divertor leg and near the strike point. The Super-X scenario

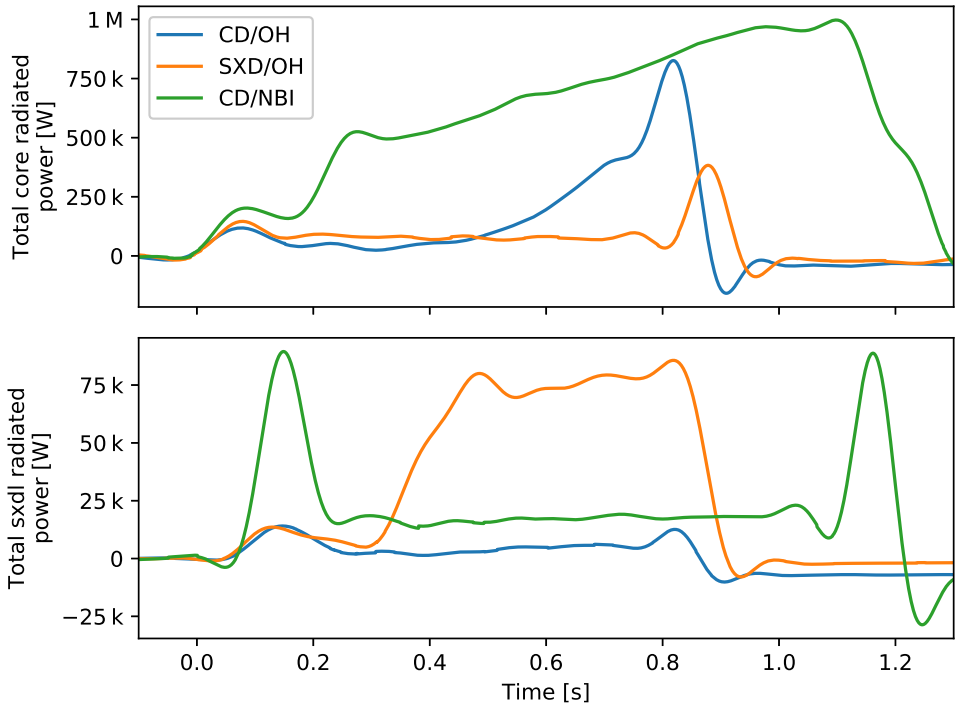

FIG. 15: Total radiated power measured by the core and lower divertor bolometer arrays. Less divertor radiation is measured in the conventional divertor (CD) plasma than the Super-X divertor (SXD) plasma. The NBI-heated plasma had significantly higher measured total radiated power than the Ohmically-heated (OH) plasmas.

shows more measured radiation, but again misses a significant amount further from the target towards the X point. Both these shots show low levels of radiated power compared with the NBI-heated scenario, as one might expect given the significant reduction in input power.

Figure 16 shows the core and divertor brightness profiles for an Ohmically-heated plasma which started in a conventional divertor configuration and transitioned to a Super-X divertor configuration, after which a small density ramp was applied from 600 ms until the end of the discharge. Despite being in a connected double null configuration, there is a significant asymmetry in the core radiation, with radiation near the top of the core plasma reducing as the divertor outer leg target radius increases from conventional to Super-X while the bottom part of the core plasma sustains about the same radiation levels. The movement of the radiation front with strike point position can also be clearly seen in the divertor profiles, though the movement stops at around 400 ms and remains somewhere around 2.7 m

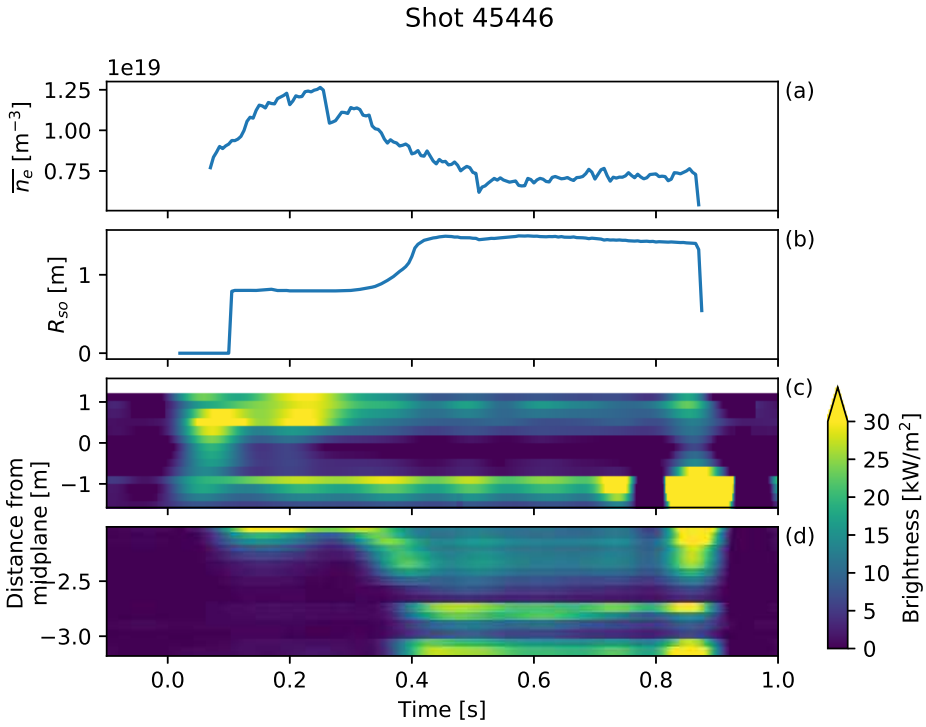

FIG. 16: Brightness profiles measured by the core poloidal (c) and lower divertor baffle-mounted (d) arrays, for an Ohmically-heated plasma which moved from a conventional divertor configuration to a Super-X configuration (b) and had a small density ramp applied during the Super-X phase (a). The poloidal array shows the degree of up/down symmetry in this connected double null plasma. The movement of the radiation front as the divertor leg sweeps out can be seen in the divertor brightness profile.

(hardware failures here limit the spatial resolution with which we can determine the position of the front). The density ramp in this shot was too small to move the radiation front further up the leg to where it could be detected by the neighbouring working bolometer channels.

C. Brightness measurements during NBI heating

As described in Section II, there are two tangentially-viewing arrays of bolometers at the midplane, viewing clockwise and counter-clockwise. During NBI heating periods, there is a significant asymmetry in the brightness measurements recorded by the bolometers, even for channels with similar viewing geometries as defined by their tangency radii. Figure 17 shows an example of this behaviour for a shot which had significant Ohmic and NBI-heated

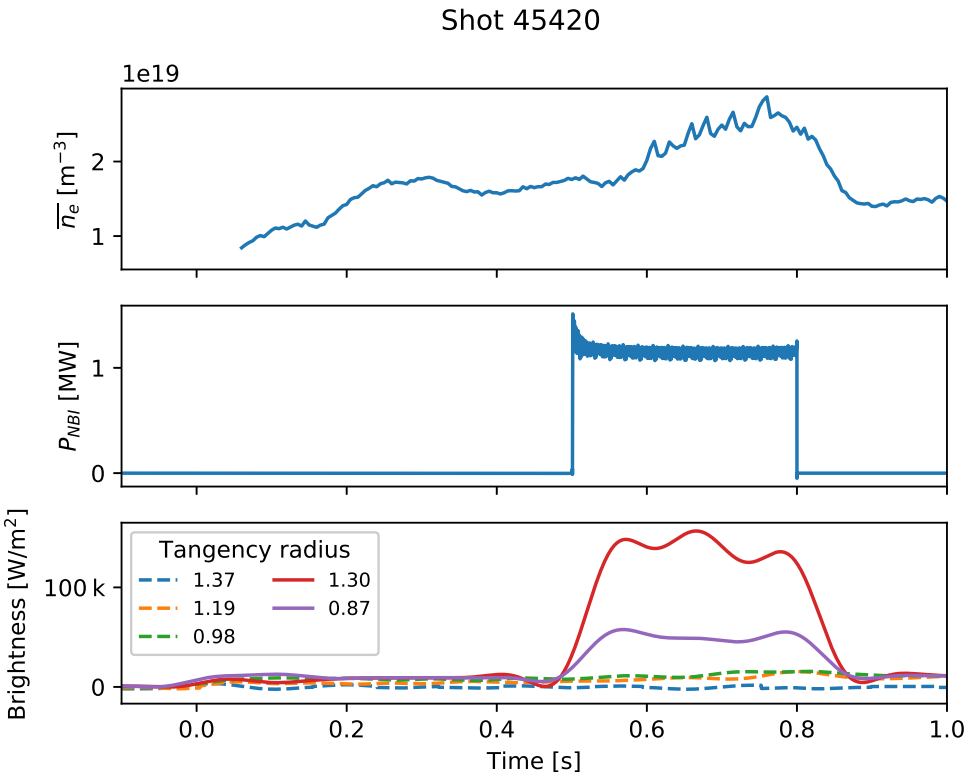

FIG. 17: Comparison of tangential bolometer signals viewing in the counter-NBI (solid) and co-NBI (dashed) direction, for a plasma with an NBI heating period. The counter-NBI-viewing channels show a large increase in signal during the period the NBI is active, but agree well with co-NBI channels at similar tangency radii during the Ohmic phase.

phases. The large increase in measured brightness of the clockwise-facing channels, by an order of magnitude, is strongly correlated with the injected beam power. The brightness levels are in good agreement before and after the beam is injected into the plasma. Note that the slow ramp up is due to smoothing of the bolometer signals and does not indicate an increase in radiation shortly before and after beam injection.

It is postulated that this significant increase in apparent brightness is due to high energy neutral particles produced by beam-plasma interactions, which are preferentially emitted in the co-beam direction. The effect is seen not only when the on-axis beam is used, but also when the off-axis beam is used which is 60° toroidally and 65 cm vertically displaced from the on-axis beam: this indicates some degree of transport of fast particles before they leave the plasma. These fast ions have large Larmor orbits that drift across the plasma cross

section into loss orbits, where they charge exchange with cold neutral atoms. The resulting fast neutrals are no longer confined and are able to reach the bolometer foils, imparting their energy onto the foils as they collide.

An important point to note about these observations is the strong toroidal asymmetry. Power balance calculations which assume toroidally-symmetric radiation losses and heat loads would likely miss this power channel loss. It is not possible to determine the total power lost through this mechanism as we are unable to confirm what fraction of the fast particles are actually being detected, but it could potentially represent a significant amount of power which would have an appreciable effect on the power balance. It could for example at least partially explain previous observations of an energy deficit on devices heated by NBI[21].

D. Electronic interference

The bolometer system has suffered from excessive noise pickup due to electro-magnetic interference in the first MAST Upgrade campaign. This has limited the time resolution achievable by the diagnostic, as heavy smoothing must be applied to achieve an acceptable signal-to-noise ratio. While the bolometer system is not the only system on MAST-U to suffer interference, the typically small signal levels (of order 1 mV) mean it has been one of the more seriously affected diagnostics.

The AC synchronous detection and high performance digital filtering performed by the ex-vessel electronics is effective at removing $1/f$ noise and sources of interference localised in the frequency domain. However, it is unable to remove broad band noise which overlaps the frequency domain in which the synchronous detection is performed. Hence, the characteristics of the interference on MAST-U limit the extent to which this interference can be removed from the signal.

Figure 18 shows the noise picked up by a typical bolometer channel, for a typical plasma shot. This data was taken with the AC synchronous detection described in Section II B disabled, so represents the raw bridge voltage pickup. The noise appears for the duration of the window when MAST-U's switched mode power supplies are enabled, from -0.8 s to 2.3 s, and is strongly correlated with this enable window. As can be seen from the zoomed time trace (b), the noise is non-sinusoidal, regular but not exactly repeatable and has a

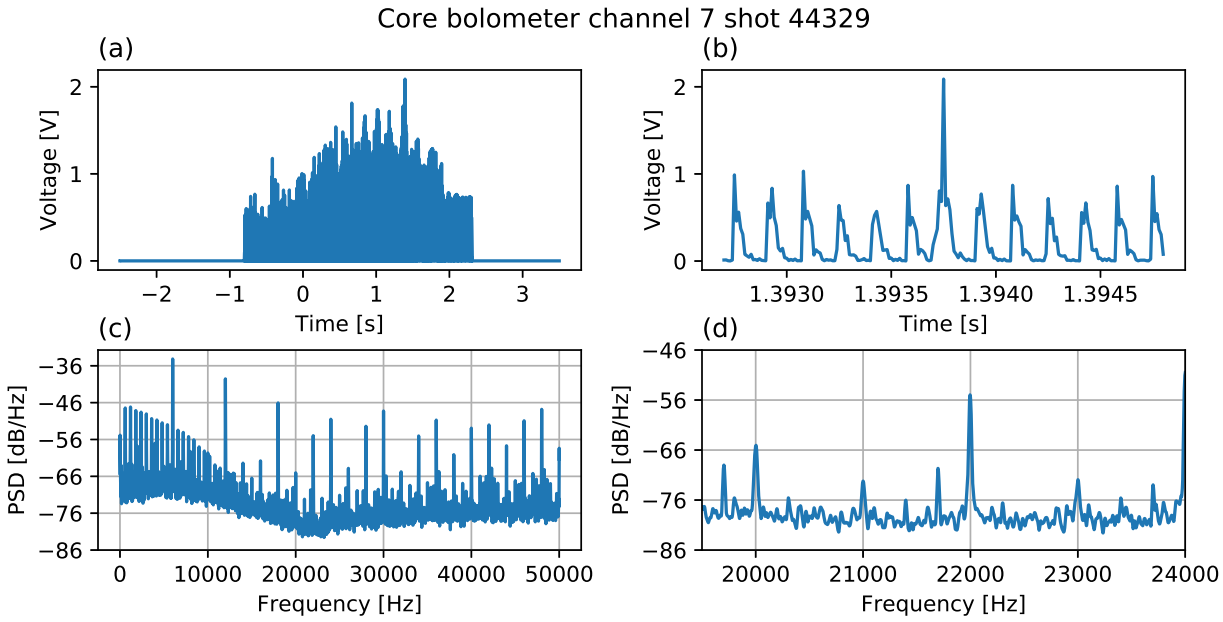

FIG. 18: Noise pickup for a typical bolometer channel in a plasma shot. Top: time series of the full shot (a) and zoomed in (b) showing the temporal evolution of the noise. Bottom: noise spectrum in the full frequency range (c) and zoomed to the region where the AC synchronous detection is typically performed (d).

rather large duty cycle of almost 50%. This makes it very difficult to use time-domain-based noise removal techniques such as spike removal.

The bottom half of Figure 18 shows the spectrum of the noise during the window the power supplies are active. It is very broad band, with many individual peaks and a noise floor significantly above that in the absence of the power supplies (which sits at around −130 dBm). Of particular note is a strong 6 kHz component with many harmonics (higher harmonics are aliased due to down-sampling required to acquire this data), corresponding to the switching frequency of MAST-U's switched mode power supplies. Efforts to identify the route by which this noise enters the bolometer electronics and devise effective hardware mitigations are underway.

We can mitigate the effect of the noise by optimising the AC synchronous detection. The choice is frequency for the excitation voltage, along with the bandwidth of the low pass filter used for the time integral, determines from which region of the spectrum the diagnostic will show noise pickup. Figure 19 illustrates this in practice: we take the previously-shown raw voltage data and apply a post-shot sinusoidal excitation voltage waveform on top, then

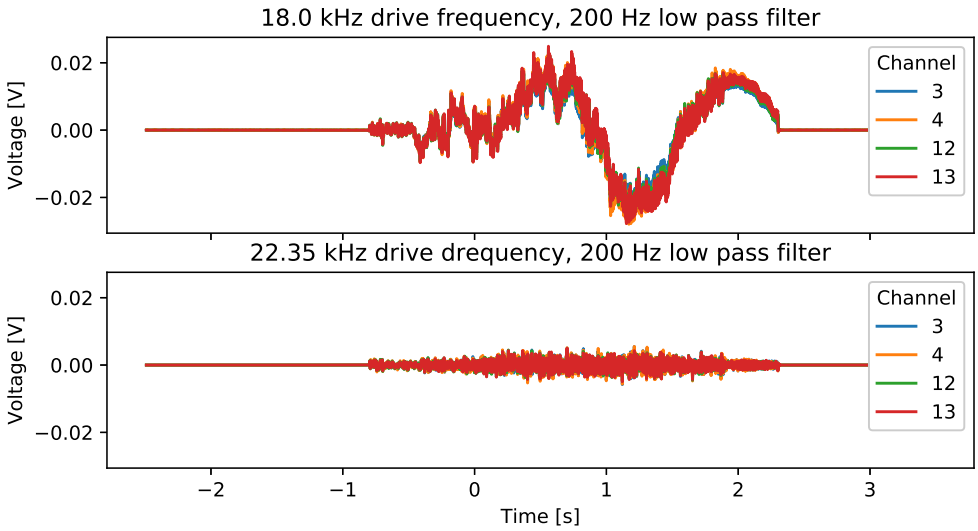

FIG. 19: Effect of drive voltage frequency on noise pickup on the demodulated bolometer signal of a selection of main chamber channels. At 18 kHz there is a large noise component, which is significantly reduced when changing the excitation frequency to 22.35 kHz.

perform the synchronous detection in software. At 18 kHz, the frequency of one of the large noise harmonics, the residual noise is as large as 20 mV, but by moving to 22.35 kHz — away from strong line noise sources in the spectrum — the residual noise is reduced by an order of magnitude. This requires no hardware changes, merely a change to the settings on the BOLO8 acquisition system.

Early in the operation of the system, it was discovered that there was a very low frequency (sub-1 Hz) beat voltage on the bolometer channels. This occurred even in shots with no power supplies enabled (such as gas calibration shots), which indicated a different source of noise to that already discussed. Investigation showed that this noise pickup was in fact coming from the other bolometer camera. An internal clock is used as a reference when generating the excitation voltage of the requested frequency. This design decision was made in order to enable to excitation voltage to be applied continually to reduce thermal cycling of the bolometers in installations where the acquisition clock is only active during the pulse sequence, but it does mean that two different ACQ2106 units will have small variations in their internal clock frequencies due to manufacturing tolerances and environmental variations.

On MAST-U, the main chamber and divertor arrays are connected to different ACQ2106

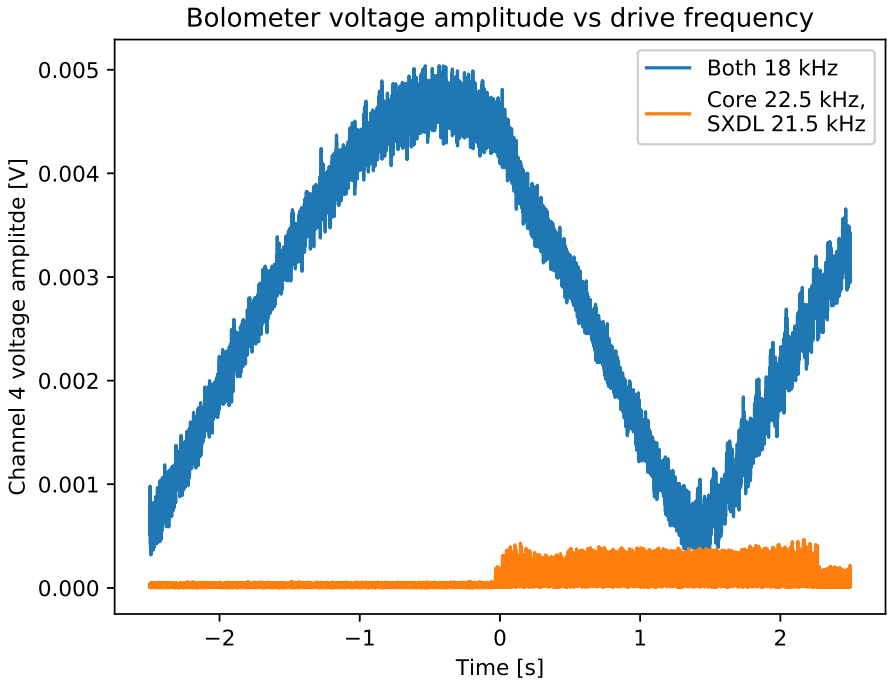

FIG. 20: Voltage amplitude in non-plasma shots, showing a beat frequency when the drive voltages of the core and SXDL systems are almost matched in frequency. By separating the drive voltage frequencies, this beat frequency is filtered out by the electronics.

units. Both were originally set to use the same excitation frequency, but in reality there was a sub-Hz difference in the frequencies of the analogue output voltages. The excitation voltage from the core system was picked up by the divertor system and vice versa, and after the AC synchronous detection was performed the frequency mismatch appeared as a low frequency beating on the measured voltages, as shown in Figure 20.

The solution adopted was to set the core and divertor systems to use different excitation frequencies, far enough apart in frequency that the digital filtering performed as part of the synchronous detection suppressed the resulting beat voltage. We set the two excitation frequencies to be a little over 1 kHz apart and set the digital filter bandwidth to 500 Hz. As can be seen in the figure, this was sufficient to eliminate the beat. The downside of this solution is that it requires two suitable frequency operating points to be available, which limits options in the high noise environment of MAST-U. An alternative solution would be to synchronise the excitation voltage to the same external clock that is used for data acquisition, which would require some firmware modifications to the BOLO8 system and

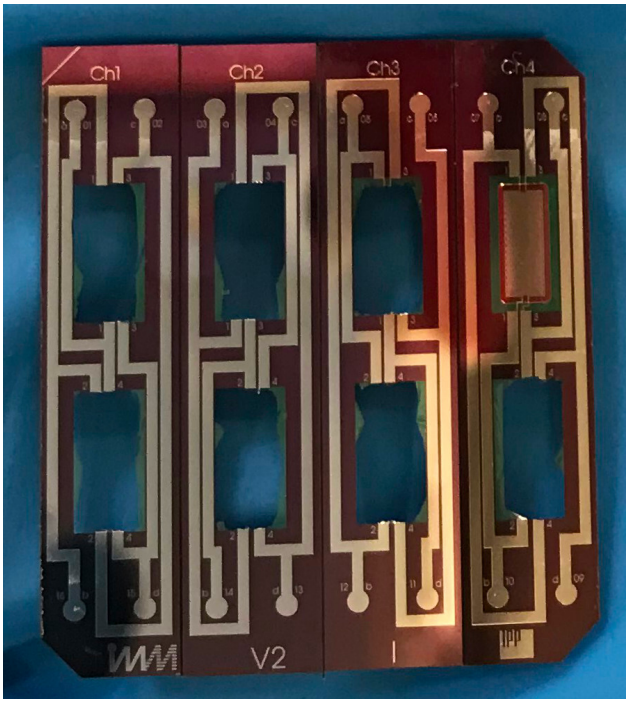

FIG. 21: One of the 4-channel bolometer chips which failed during the campaign. The foils have been destroyed, leaving a ragged edge. Only one of the 8 foils in this chip survived.

careful treatment of the situation where the acquisition clock is intermittent.

E. Failures of in-vessel detectors

After approximately 2 months of routine operations, failures of the wall-mounted divertor bolometer channels were observed. This was first noticed by failure of the routine calibration performed before every shot, as described in Section III A. Subsequent measurements of inter-pin resistances on the vacuum feedthroughs on the vessel showed pins which should have been connected across the bridge having open circuit resistances. This failure severely limited the capability of the divertor bolometer system and precluded performing tomographic inversions of the radiation emissivity profile, as well as limiting measurements of the radiation in conventional divertor configuration plasmas.

During the engineering break after the end of the first experimental campaign, the wall-mounted divertor bolometer camera was removed from the vessel, disassembled and inspected. It was noticed that the measurement foils appeared to be missing from the bolometer chips, and upon disassembling one of the sensors and extracting the chips it was

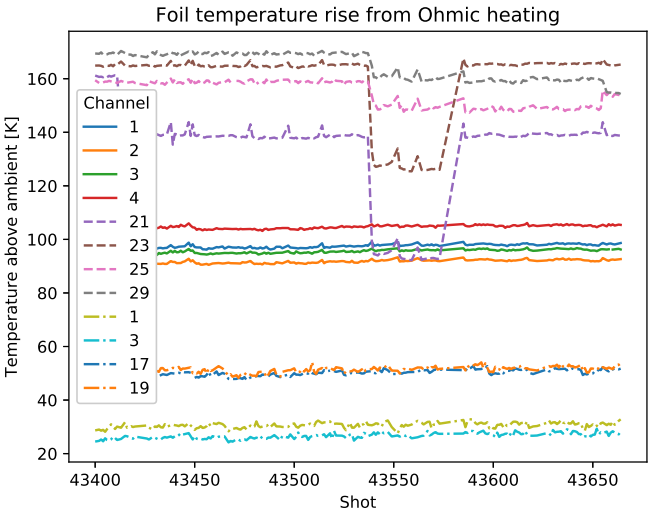

FIG. 22: Bolometer foil temperature rise due to Ohmic heating by the excitation voltage. Solid lines: baffle-mounted divertor channels. Dashed lines: wall-mounted divertor channels. Dash-dotted lines: main chamber channels. The wall mounted divertor channels run considerably hotter than either the baffle-mounted or main chamber channels.

ascertained that the foils had broken away from the chips, as shown in Figure 21. In this figure all but one of the foils in the 4-channel collection of chips failed, leaving a ragged edge where the foil assembly was stretched across and suspended in place.

Failure due to mechanical shock was ruled out: the foils were designed to withstand greater shocks than the camera had been subjected to during the campaign. A pressure differential causing an unacceptably high force normal to the foil face and pushing the foils out was also considered, but the scale and speed of pressure changes in the divertor during plasma operations is insufficient to cause this failure, and the foils survived the (two) initial pump downs from air pressure to a vessel pressure of 1×10^{-8} mbar unscathed. Fatigue from thermal cycling due to plasma radiation was also considered, but the level and duration of radiative power loads on these foils in MAST-U plasmas would have only resulted in about a 1 K temperature rise.

It was ultimately determined that the foils were suffering thermally-induced failures due to elevated operating temperatures, which is generally more of a concern for bolometers used in long-pulse or reactor environments. Using the measured DC current and voltage in the calibration, it is possible to estimate the resistance of the meander resisters through which

the current is flowing, which will to a good approximation be the same as the resistance of all 4 bridge resisters, using simply $R_{foil,active} = V_{DC}/I_{DC}$. The resistance of the foils with no current $R_{foil,idle}$ was measured regularly throughout the campaign using a multimeter attached to the vacuum feedthrough socket. Along with the temperature coefficient of resistance α we can determine the temperature rise of the meander resistors (and hence the foils) via the simple relation:

$$\Delta T = \alpha(R_{foil,active} - R_{foil,idle}) \tag{10}$$

We take $\alpha = 2.4 \times 10^{-3}\,\Omega/\mathrm{K}$, which is a little bit lower than values found in the literature for platinum but similar to those measured during manufacture of this type of bolometer chip[22]. The calculated temperature rise is shown in Figure 22, for a representative sample of baffle-mounted divertor, wall-mounted divertor and main chamber channels. The main chamber channels run coolest as their intrinsic resistance is higher and so the Ohmic heating current is lower. The baffle mounted channels have a 175 nm Al heat conducting layer applied to improve thermal conductivity between the foils and the heat sink, which also helps them run cooler. The wall mounted sensors do not have this layer, and this means they run significantly hotter, at up to 160 K above ambient temperature. Allowing for a range of α of $2.1 \times 10^{-3}\,\Omega/\mathrm{K}$ to $2.6 \times 10^{-6}\,\Omega/\mathrm{K}$, resulting from iterative improvements to the manufacturing process over the time range this bolometer chip type was manufactured[22] gives a corresponding temperature rise of between 150 K and 190 K for the wall-mounted foils. At ambient temperatures of 20 °C this means the foils are operating at around 200 °C, which has been shown to lead to premature failure in testing[23]. We therefore theorise that it is these elevated operating temperatures which caused the premature failure of these sensors.

The failed bolometer chips were replaced and the sensors reinstalled in the vessel during the engineering break. In order to reduce the risk of a repeat of these failures, we have replaced the chips with ones which do feature the heat conduction layer, which should reduce the operating temperature. As an additional precaution we have halved the amplitude of the excitation voltage, which will reduce the Ohmic heating by a factor of 4 and should greatly reduce the operating temperature. This does come at the expense of signal levels, so we hope to raise the voltage amplitude back up to the maximum after demonstrating the operating temperature is safe.

IV. OUTLOOK

Despite the challenges encountered during the first MAST-U experimental campaign, the bolometer system has produced useful measurements of the radiated power which are enabling analysis of a range of experiments. Using knowledge gained from these early operations, a number of improvements have been or are planned to be implemented.

Repairs to failed channels and adopting a more cautious operating regime should enable us to achieve the full spatial resolution for which the system was designed, and infer information about the radiation emissivity profile in the lower divertor using the tools described in Section II C. Modifications to the ex-vessel cabling and earthing have been made during the engineering break with the aim of reducing the electrical interference, in parallel with investigative work on the reducing the noise at its source. This work should help to improve the achievable time resolution of the system with acceptable signal-to-noise ratio.

To address the lack of coverage of the lower X point, development of integrated analysis techniques using the resistive bolometers and MAST Upgrade's infra-red video bolometer (IRVB), which has a viewing geometry optimised for X point coverage, will be developed. This should provide better estimates of the total radiated power than either diagnostic can achieve in isolation.

Finally, a new bolometer camera has been installed in the upper divertor. This new camera is designed so that the lines of sight mirror those of the wall-mounted lower divertor camera, as shown in Figure 23. By designing the camera to have the same viewing geometry relative to the divertor leg in both the upper and lower divertors, we can make measurements of the up/down radiation asymmetry by comparing both the line-integral brightness profiles and an estimate of the total divertor radiated power. The camera is located in sector 1, the same as the main chamber arrays and immediately adjacent to sector 12 where the lower divertor bolometer are located, to minimise the impact of any toroidal asymmetries (particularly during transient events).

The camera design is based on that of the lower divertor, as shown in Figure 24 for comparison with Figure 3. Modifications to the design were required to permit a different mounting position resulting from the different locations of port on the upper and lower halves of the machine: the lower bolometer is mounted to the port plate, whereas the upper bolometer is mounted directly on the vacuum vessel inner wall. The new camera does

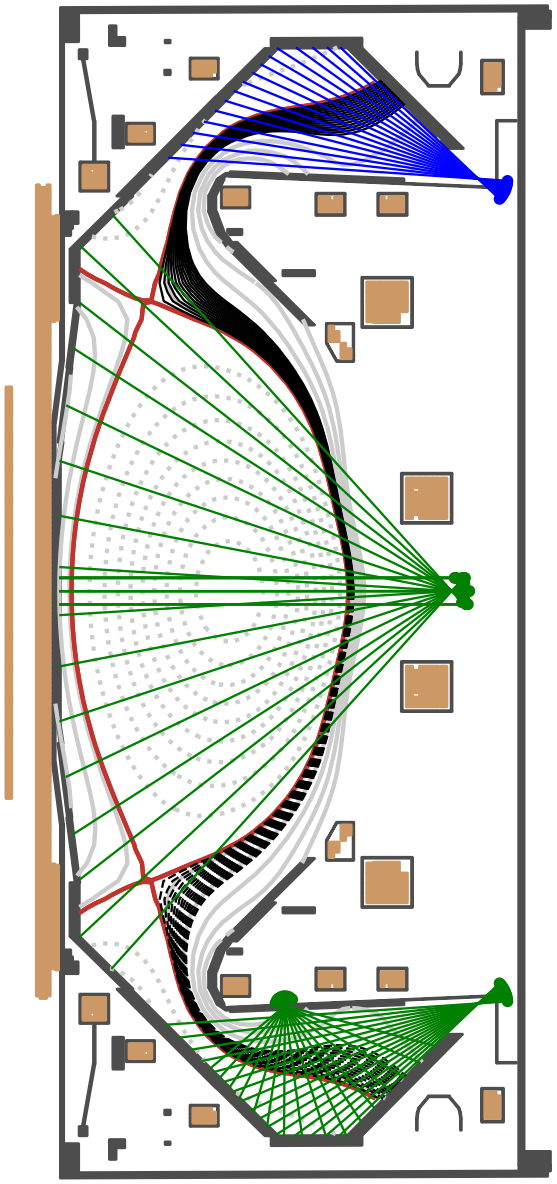

FIG. 23: Poloidal lines of sight of the bolometer system for the second campaign, including the new upper bolometer (blue).

however feature the same sensor arrangement, aperture shape and anti-reflection internal components as the lower camera. The sensors used feature gold foils; this does pose a challenge for interpretation as the different reflectivity of platinum and gold in the lower and upper divertors respectively at low photon energies must be accounted for. However, it was decided that the less brittle gold foils represented a lower risk of failure than the platinum foils, and the interpretation complexity was considered an acceptable price to pay

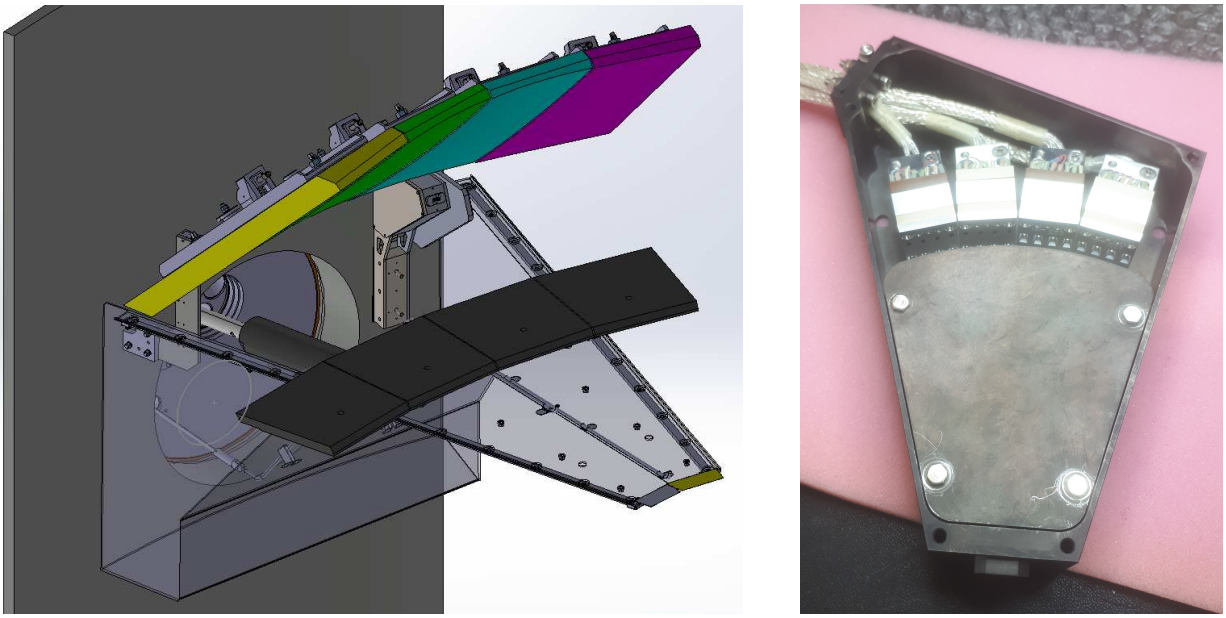

FIG. 24: Left: the position of the upper bolometer camera in the vessel, shown by a CAD representation of the camera and surroundings. The camera is bolted to a plate which is in turn welded to the vessel wall, unlike the lower camera which is bolted to the port plate. Right: the new camera during assembly, showing the modified shape to enable it to fit against the vessel wall while maintaining the same sensor positions relative to the divertor as those in the lower wall-mounted bolometer camera.

for what is expected to be improved robustness of the system.

As well as direct up/down radiation asymmetry measurements, the addition of the upper divertor bolometers improves the ability to perform whole device power balance measurements. Radiation in the upper divertor is likely to be a significant power loss mechanism in many MAST-U plasmas, particularly up/down symmetric double null and upper single null Super-X plasmas which are standard MAST-U operating scenarios, so this new installation contributes significantly towards the goal of full device radiation coverage. With the main chamber, lower divertor, upper divertor and IRVB diagnostics, the whole plasma poloidal cross section has radiated power coverage with the exception of the upper X point. Future diagnostic development will prioritise adding this last piece of required coverage.

V. SUMMARY

MAST Upgrade features a resistive bolometer system to measure the spectrally-integrated power radiated by the plasma. A poloidal array in the main chamber measures the core plasma radiation and up/down asymmetries, while tangential arrays provide radial profiles of the core radiation. Two arrays of bolometers in the lower divertor chamber provide measurements of the divertor radiation and can be inverted to produce 2D poloidal emissivity profiles. Bolometer measurements are digitised using FPGA-based smart, compact electronics units.

The main chamber and lower divertor systems were commissioned for the first experimental campaign, and provided routine radiated power measurements. Difficulties were encountered with high noise levels and in-vessel hardware failures, with investigation, repair and mitigation undertaken throughout the campaign and during the engineering break after the end of the campaign.

The repaired lower divertor system is complemented by a new upper divertor camera, providing up/down asymmetry measurements and improved whole-device radiated power measurements.

ACKNOWLEDGMENTS

This work is supported by US Department of Energy awards DE-AC05-00OR22725 and DESC0014264. This work has been part-funded by the EPSRC Energy Programme (grant numbers EP/T012250/1 and EP/W006839/1). To obtain further information on the data and models underlying this paper please contact PublicationsManager@ukaea.uk. Support for M. L. Reinke's contributions was in part provided by Commonwealth Fusion Systems. The authors would like to thank Stefan Schmitt, Hans Meister and Matthias Bernert for discussions of possible failure modes of the sensor shown in Section III E.

REFERENCES

[1]M. Wischmeier, "High density operation for reactor-relevant power exhaust," Journal of Nuclear Materials **463**, 22–29 (2015), Plasma-Surface Interactions 21.

[2]W. Biel, M. de Baar, A. Dinklage, F. Felici, R. König, H. Meister,

W. Treutterer, and R. Wenninger, "DEMO diagnostics and burn control," Fusion Engineering and Design **96-97**, 8–15 (2015), proceedings of the 28th Symposium On Fusion Technology (SOFT-28).

[3]F. Federici, M. L. Reinke, B. Lipschultz, A. J. Thornton, J. R. Harrison, J. J. Lovell, P. Ryan, M. Bernert, H. F. Meyer, and the MAST Upgrade Team, "Design and implementation of a prototype infrared video bolometer (IRVB) in MAST Upgrade," Review of Scientific Instruments (In review).

[4]K. F. Mast, J. C. Vallet, C. Andelfinger, P. Betzler, H. Kraus, and G. Schramm, "A low noise highly integrated bolometer array for absolute measurement of VUV and soft x radiation," Review of Scientific Instruments **62**, 744–750 (1991), https://doi.org/10.1063/1.1142078.

[5]H. Meister, M. Bernert, W. Biel, M. Han, L. Ingesson, K. Mukai, F. Penzel, B. Peterson, R. Reichle, M. Reinke, S. Schmitt, and D. Zhang, "Bolometer developments in diagnostics for magnetic confinement fusion," Journal of Instrumentation **14**, C10004–C10004 (2019).

[6]H. Meister, M. Willmeroth, D. Zhang, A. Gottwald, M. Krumrey, and F. Scholze, "Broad-band efficiency calibration of ITER bolometer prototypes using Pt absorbers on SiN membranes," Review of Scientific Instruments **84**, 123501 (2013), https://doi.org/10.1063/1.4834755.

[7]U. A. Sheikh, B. P. Duval, B. Labit, and F. Nespoli, "A novel carbon coating technique for foil bolometers," Review of Scientific Instruments **87**, 11D431 (2016), https://aip.scitation.org/doi/pdf/10.1063/1.4961271.

[8]A. Huber, K. McCormick, P. Andrew, P. Beaumont, S. Dalley, J. Fink, J. Fuchs, K. Fullard, W. Fundamenski, L. Ingesson, F. Mast, S. Jachmich, G. Matthews, P. Mertens, V. Philipps, R. Pitts, S. Sanders, and W. Zeidner, "Upgraded bolometer system on JET for improved radiation measurements," Fusion Engineering and Design **82**, 1327–1334 (2007), proceedings of the 24th Symposium on Fusion Technology.

[9]A. Y.-C. Yu, W. E. Spicer, and G. Hass, "Optical properties of platinum," Phys. Rev. **171**, 834–835 (1968).

[10]J. Lovell, G. Naylor, A. Field, P. Drewelow, and R. Sharples, "An FPGA-based bolometer for the MAST-U Super-X divertor," Review of Scientific Instruments **87**, 11E721 (2016), https://aip.scitation.org/doi/pdf/10.1063/1.4961556.

[11]J. Lovell, *Development of Smart, Compact Fusion Diagnostics using Field-Programmable Gate Arrays*, Ph.D. thesis, Durham University, Centre for Advanced Instrumentation, Department of Physics, South Road, Durham, DH1 3LE (2017).

[12]M. Carr, J. Lovell, M. Tomes, V. Neverov, D. A. Meakins, K. Munechika, D. Stańczak, and D. Bold, "cherab/core: Release v1.3.0," (2021).

[13]M. Carr, A. Meakins, M. Bernert, P. David, C. Giroud, J. Harrison, S. Henderson, B. Lipschultz, and F. Reimold, "Description of complex viewing geometries of fusion tomography diagnostics by ray-tracing," Review of Scientific Instruments **89**, 083506 (2018), https://doi.org/10.1063/1.5031087.

[14]L. C. Ingesson, "Comparison of methods to determine the total radiated power in JET," JET technical report JET-R(99)06 (JET Joint Undertaking, 1999).

[15]J. Lovell, M. L. Reinke, U. A. Sheikh, R. Sweeney, P. Puglia, P. Carvalho, and L. Baylor, "Methods to determine the radiated power in SPI-mitigated disruptions in JET," Review of Scientific Instruments **92**, 023502 (2021), https://doi.org/10.1063/5.0014654.

[16]C. Groetsch, "The theory of Tikhonov regularization for Fredholm equations," 104p, Boston Pitman Publication (1984).

[17]D. Moulton, B. Lipschultz, and J. Harrison, "Detachment onset in MAST-U according to SOLPS-ITER," in *44th EPS Conference on Plasma Physics* (2017) pp. 1–45.

[18]L. Ingesson, "The mathematics of some tomography algorithms used at JET," JET technical report JET-R(99)08 (JET Joint Undertaking, 2000).

[19]J. Weese, "A reliable and fast method for the solution of Fredhol integral equations of the first kind based on Tikhonov regularization," Computer Physics Communications **69**, 99–111 (1992).

[20]R. Sano, M. Fukumoto, T. Nakano, and N. Oyama, "New design techniques of resistive bolometer system for analysis of total radiated power," Review of Scientific Instruments **89**, 083501 (2018), https://doi.org/10.1063/1.5026927.

[21]G. Matthews, S. Silburn, C. Challis, T. Eich, D. Iglesias, D. King, B. Sieglin, and J. Contributors, "Dynamic power balance analysis in JET," Physica Scripta **2017**, 014035 (2017).

[22]H. Meister, Email correspondance.

[23]H. Meister, M. Kannamüller, J. Koll, A. Pathak, F. Penzel, T. Trautmann, P. Detemple, S. Schmitt, and H. Langer, "Reliability issues for a bolometer detector for ITER at high operating temperatures," Review of Scientific Instruments **83**, 10D724 (2012),

https://doi.org/10.1063/1.4740256.